Received: 30 December 2022 | Revised: 6 June 2023 | Accepted: 20 June 2023

DOI: 10.1002/mp.16622

RESEARCH ARTICLE

MEDICAL PHYSICS

Sound speed and attenuation of human pancreas and pancreatic tumors and their influence on focused ultrasound thermal and mechanical therapies

Michael D. Gray | **Laura Spiers** | **Constantin C. Coussios**

Institute of Biomedical Engineering, University of Oxford, Oxford, UK

Correspondence
Michael D. Gray, Institute of Biomedical Engineering, University of Oxford, Oxford, OX3 7LD, UK.
Email: michael.gray@eng.ox.ac.uk

Abstract

Background: There is increasing interest in using ultrasound for thermal ablation, histotripsy, and thermal or cavitational enhancement of drug delivery for the treatment of pancreatic cancer. Ultrasonic and thermal modelling conducted as part of the treatment planning process requires acoustic property values for all constituent tissues, but the literature contains no data for the human pancreas.
Purpose: This study presents the first acoustic property measurements of human pancreatic samples and provides examples of how these properties impact a broad range of ultrasound therapies.
Methods: Data were collected on human pancreatic tissue samples at physiological temperature from 23 consented patients in cooperation with a hospital pathology laboratory. Propagation of ultrasound over the 2.1–4.5 MHz frequency range through samples of various thicknesses and pathologies was measured using a set of custom-built ultrasonic calipers, with the data processed to estimate sound speed and attenuation. The results were used in acoustic and thermal simulations to illustrate the impacts on extracorporeal ultrasound therapies for mild hyperthermia, thermal ablation, and histotripsy implemented with a CE-marked clinical system operating at 0.96 MHz.
Results: The mean sound speed and attenuation coefficient values for human samples were well below the range of values in the literature for non-human pancreata, while the human attenuation power law exponents were substantially higher. The simulated impacts on ultrasound mediated therapies for the pancreas indicated that when using the human data instead of the literature average, there was a 30% reduction in median temperature elevation in the treatment volume for mild hyperthermia and 43% smaller volume within a 60°C contour for thermal ablation, all driven by attenuation. By comparison, impacts on boiling and intrinsic threshold histotripsy were minor, with peak pressures changing by less than 15% (positive) and 1% (negative) as a consequence of the counteracting effects of attenuation and sound speed.
Conclusion: This study provides the most complete set of speed of sound and attenuation data available for the human pancreas, and it reiterates the importance of acoustic material properties in the planning and conduct of ultrasound-mediated procedures, particularly thermal therapies.

KEYWORDS
ablation, human, hyperthermia, pancreas, ultrasound

1 | INTRODUCTION

The pancreas has long been an intriguing target for ultrasound therapies, both as a potential replacement for surgery and as a means of enhancing drug-based treatments used in neoadjuvant or palliative care settings. Regardless of therapeutic approach, the anatomical location of the pancreas creates challenges for safe delivery of ultrasound. It is one of deeper locations within the body that can potentially be treated with ultrasound, with propagation depths that could exceed 10 cm.[1] Distinguishing it from the inferior border of the stomach can be difficult due to the lack of pancreatic capsule.[2] Identifying tumors accurately within the pancreas can be complicated by the varying echogenicity associated with age and adiposity.[3] Once visualized, delivery of ultrasound to pancreatic ductal adenocarcinomas (PDAC) must consider adjacent gas-filled structures such as the proximal duodenum and stomach, whilst avoiding critical vasculature such as the splenic artery crossing the pancreatic tail. Although a retroperitoneal organ, the pancreatic head may move cranio-caudally up to 7.6 mm ± 3 mm during respiration.[4]

High-intensity focused ultrasound has long been contemplated as a non-invasive alternative to high-risk surgical resection. Despite its retroperitoneal position and proximity to major structures, the pancreas can be directly targeted with focused ultrasound, and ablation of pancreatic tumors has been performed safely.[5] This approach uses the thermal and cavitational effects of focused ultrasound (FUS) beams with powers in the hundreds of Watts for direct tumor destruction. More recently, the potential of purely cavitation-based tumor liquefaction, also known as histotripsy, has been explored pre-clinically[6] and is highly likely to translate clinically in the near future.[7] Even though it presents substantial advantages in terms of the absence of thermal effects and the ease of real-time treatment monitoring using conventional B-mode imaging, histotripsy of the pancreas presents the additional challenge of needing to deliver much higher pulse average powers of over 1 kW and peak negative pressures up to 28 MPa,[8] rendered difficult by non-linearity in the lengthy tissue path and the limited acoustic window through the abdomen.

Ultrasound also has a significant role to play as an adjunct to drug delivery. In the very difficult-to-treat PDAC, systemically administered intratumoral drug delivery is limited by abundant desmoplastic stroma, which raises interstitial pressure to cause vascular collapse and limit tumor perfusion.[9] The combination of systemically administered microbubbles with chemotherapy has been recently shown to enable increased penetration of cancer therapeutics through the stromal layer, potentially demonstrating the value of these drug delivery strategies and leading to enhanced therapeutic outcomes.[10] Thermal effects of ultrasound can also be exploited to improve blood flow through tumor vasculature vasodilation induced by localized heating has demonstrated enhanced drug delivery in animal models and human trials.[11–14, 15] Combining hyperthermia with thermosensitive drugs for targeted release of cytotoxic agents is helping to address limitations of PDAC therapy.[15,16]

Trials of generating hyperthermia in PDACs have included radiowave,[17] microwave,[18] and focused ultrasound guided by magnetic resonance imaging (MRI)[19] or diagnostic ultrasound.[20] Brief temperature increases up to 42°C can be generated by FUS, with spatial peak temporal average intensities (I_{spta}) between 50–500 W/cm^2.[21] The benefits of FUS for warming tissues compared to other approaches is that it is relatively quick, inexpensive, and less invasive. Temperature elevations can be anatomically registered using an MR guided system.[22,23] However, MR-guided FUS systems are expensive and have limitations with respect to motion and monitoring in adipose tissue.[24,25] An alternative is to use an ultrasound-guided system, but there is no clinically reliable way to accurately measure the modest temperature elevations.

FUS-mediated mild hyperthermia can be combined with invasive thermometry monitoring, and this has been used to validate predictive models defining treatment parameters in the treatment of liver tumors as part of the TARDOX trial.[26] In that first-in-human study, focused ultrasound coupled to a B-mode US system simultaneously delivered treatment and guidance to investigate the safety and feasibility of drug release from thermosensitive liposomes (ThermoDox®, Celsion Corporation, USA) to tumors in the liver. Treatment plans were constructed using anatomical data from radiological imaging along with acoustic and thermal properties for the constituent tissues. With these inputs, the model predicted acoustic pressures and temperature maps in the target tumor and generated personalized ultrasound treatment plans for enhanced localized drug delivery.[27] The TARDOX trial compared patients monitoring with invasive thermometry to those treated using a modelling-only approach and observed comparable enhancements in drug delivery.

The PanDox trial[28] was a Phase I trial investigating delivery of ThermoDox® to non-resectable PDACs, using FUS-induced mild hyperthermia (>39.5°C). The treatment concept was ultrasound guided and thermometry-free, so it was critical that the model incorporate accurate acoustic and thermal properties in order to maximize the likelihood of a safe and efficacious treatment without the need for invasive or MR thermometry. The PanDox trial therefore required a

modified version of the validated TARDOX treatment planning model to translate FUS exposure parameters for hyperthermia from the liver to the pancreas. Unfortunately, review of the relevant literature showed scarce data availability for the pancreas, primary in bovine and porcine samples.[29–31]

Pancreas acoustic properties may influence candidate ultrasound-mediated therapies in several ways. Sound speed contrast with surrounding tissues may manifest through refraction and modest amplitude changes in the transmitted sound. Attenuation may alter the amplitude of the transmitted beam, although given the depth of the organ, lower frequencies are likely to be used for extracorporeal sources and the attenuation losses should be modest through the relatively small thickness of the organ. A greater effect may appear in the linear heating rate for a target at a distance z inside the pancreas:

$$\dot{q} = 2aI = (2a/\rho c)\left\langle p_T^2 \right\rangle e^{-2\alpha z} \quad (1)$$

with defining parameters of density (ρ), sound speed (c), time-average of the squared pressure transmitted through the pancreas $\langle p_T^2 \rangle$, attenuation (α), and absorption (a). To first order, the latter two are approximately equal, with the justification that the scattering contribution to total attenuation may be locally absorbed.[32] For numerical example, if the attenuation/absorption was lowered from 0.10 np/cm to 0.05 np/cm without changing any other values, the heating rate would drop by a factor of 1.81 for a 1-cm propagation distance through the pancreatic tissue. By comparison, the sound speed would not be expected to vary beyond 3%, and its impact on Equation (1) is effectively neutralized between the transmission coefficient for adjoining tissues and the explicit speed in the denominator. The absorption-driven change in heating rate will also be present in the generation of radiation force per unit volume[33] ($F_V = \dot{q}/c$).

When the ultrasound field is nonlinear, the influence of attenuation may be even greater due to enhanced energy absorption at harmonic frequencies. This in turn leads to increases in heating[34] and force generation,[35] and in the case of boiling histotripsy, facilitates vapor bubble formation from shock front heating.[36,37] In intrinsic threshold histotripsy,[7,8] higher attenuation may inhibit the ability to achieve the rarefactional pressures required to initiate cavitation.

Given the potential impact of the acoustic properties on pancreatic therapies and the dearth of relevant results in the literature, a study was undertaken to collect data on freshly excised human tissues. This manuscript describes methods for data collection, presents results for sampled tissues, and demonstrates the impact of the newly gathered information on both mild hyperthermic and ablative therapies.

2 | METHODS

2.1 | Protocol

Human pancreatic tissue samples from consented patients were obtained post-surgery in co-operation with a hospital pathology laboratory and tissue bank (project number 19/A100, under Oxford Radcliffe Biobank Research Tissue Bank ethical approval). Anonymized resected specimens were provided within 3 h of excision and remained unfixed. They were first prepared by a trained pathologist, initially with gentle palpation and visual assessment. The organs were then stained to mark key structures for later orientation during histological evaluation and partially sliced for further examination and biopsy collection. Slice separations were typically 10–20 mm thick, making for convenient cross sectional ultrasonic scans (Section 2.3). Data collection was non-destructive, and no additional procedures were required from patients, surgeons, or pathologists.

2.2 | Instrumentation

A set of ultrasonic callipers[37,38] (Figure 1A) was developed for characterizing attenuation and sound speed. The design features a pair of ¼″ diameter, 3.5 MHz centre frequency unfocused transducers (Panametrics V384, Keymed, Southend-on-Sea, UK) that are coaxially aligned when mounted on linear digital calipers (CD-15DAX, Mitutoyo, Andover, UK). During each measurement, one of the transducers was driven with a pulser/receiver (Panametrics 500PR, Olympus NDT), and the signal transmitted through the material sample was received with the other transducer. Received signals were amplified and filtered by the pulser before digitization on a USB oscilloscope (HS5, TiePie Engineering, Sneek, Netherlands) and storage on a laptop computer. Acquisition timing was triggered using the sync output from the pulser. Sample surface temperature was monitored with a K-type thermocouple integrated into the caliper system and tracked using a digital thermometer (model 52 II, Fluke, Stockton-On-Tees, UK). Material sample thicknesses were reported by the calipers with 0.01 mm resolution.

The use of short, broadband pulse signals provided by the ultrasonic pulser was expedient relative to making equivalent measurements with a series of tone pulses whilst eliminating potential complexities from reverberation. The combined compactness of the system and the speed with which a data set could be collected were both highly advantageous for enabling this study to take place in a busy pathology department that needed to process and store samples with minimal interruption. The pulser was driven at its lowest level to minimize the likelihood and influence of nonlinearity

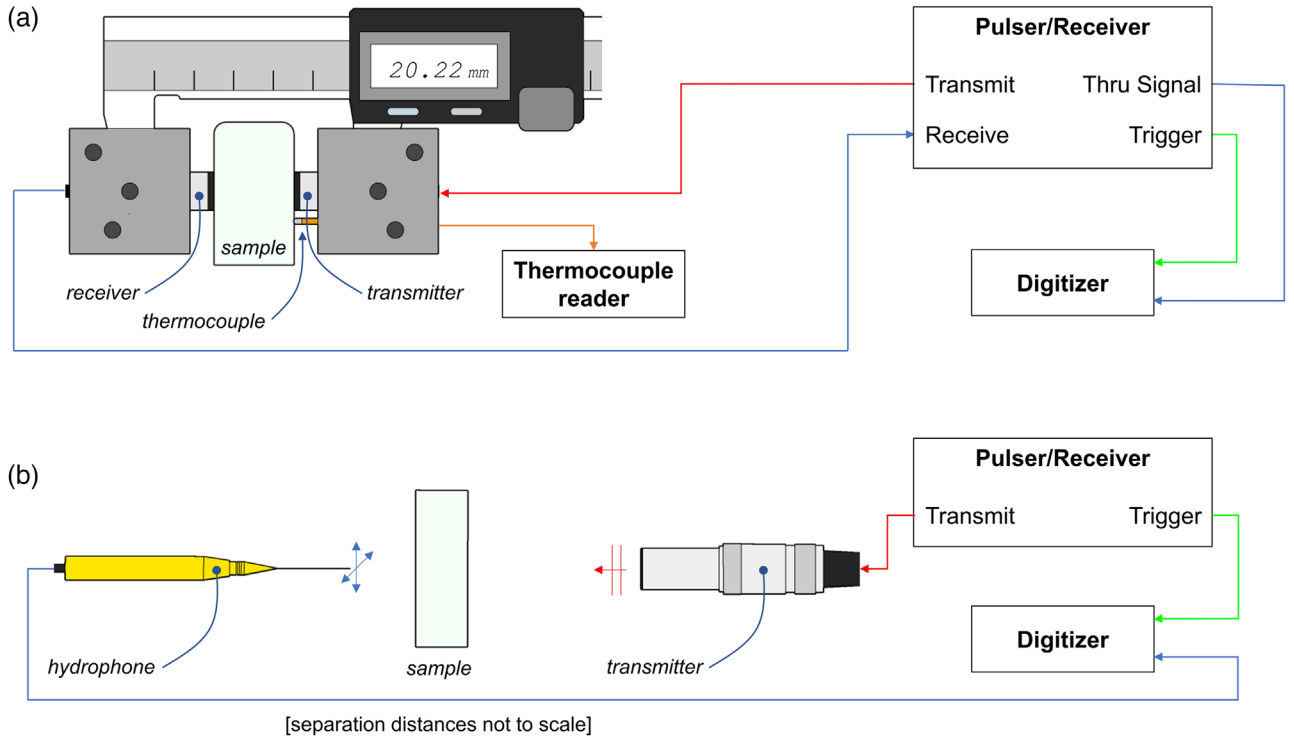

FIGURE 1 Instrumentation for (A) caliper and (B) long path measurements. The sample and the transducers are all immersed in a warm water bath (not shown). Digitizer signals were saved on a laptop computer for subsequent analysis.

on the measurements, as assessed by reviewing the signals in water. Calibration of the transmitted field in water with a needle hydrophone showed peak negative pressures no larger than 0.17 MPa.

2.3 | Measurement procedures

Once sectioning and sampling were completed by the pathologist, the pancreas specimen was placed in a bath of warm tap water maintained between 36–38°C as monitored with a digital thermometer (TP3001, METRIA, China). The pancreas was allowed to acclimatize for at least five minutes. It was lightly palpated to purge any gas released due to autolysis, although in practice, evidence of gas was rarely seen. A section of tissue was placed between caliper-mounted transducers, gently agitating to dislodge any trapped air, and taking care to avoid any punch biopsy sites (where tissue had been removed).

Transmission data through the tissue was collected, noting the tissue temperature and sample thickness for each reading. All measurements were performed in pairs, with each tissue acquisition followed by a companion measurement in the bath water using the same distance between transducers. Collection of data to include a reference water path allows for minimization of internal system biases in the calculation of sound speed and attenuation that may otherwise be present if making absolute level measurements with the tissue samples alone. The water was refreshed when the temperature fell below physiological range or when the presence of tissue debris interfered with the signal path.

2.4 | Data processing

Sound speed estimates for each sample were calculated as a function of frequency using:

$$c\ (f_m) = \left({}^{1}/_{c_{water}} + \frac{\Delta t_m}{h} \right)^{-1} \quad (2)$$

where c_{water} is the water sound speed at the measured temperature, found from a published speed-temperature relation,[39] h is the sample thickness reported by the callipers, and Δt_m is the delay between the water and tissue received signals. This delay is found from a cross correlation of both signals after filtering with a 1-MHz bandpass of center frequency f_m. The filtration step is intended to mitigate timing errors due to degraded signal coherence that could arise from correlating unattenuated (water) and attenuated (tissue) signals. Calculations were performed for a range of center frequencies spanning the receive band of 2.1 – 4.5 MHz in 100 kHz steps. In practice, the frequency

dependence was found to be negligible, and for this reason sound speed is reported as a band average for each sample.

The frequency range mentioned above was applied across all data sets as a trade-off between errors at the ends of the band, where there is already signal roll-off due to the finite bandwidth of the transducers. At higher frequencies, thicker samples will have poor signal to noise ratio, and at low frequencies, thinner samples will be insensitive to the small through-transmission losses.

Attenuation estimates for each sample were made as a function of frequency using the magnitude ratio of the water $s_{water}(f)$ and tissue $s_{tissue}(f)$ signal spectra:

$$\alpha_{tissue}(f) = \ln\left(\left|s_{water}(f)/s_{tissue}(f)\right|\right)/h + \alpha_{water}(f) \quad (3)$$

where $\alpha_{water}(f)$ is the attenuation in water.[40] The signal spectra are calculated with a Fourier transform after high pass filtering at 300 kHz to remove any DC offset and windowing around the direct path to minimize noise in the pulsed signal analysis.

The attenuation spectra were fitted to a power law expression ($\alpha_{fit} = \alpha_0 f^n$) both to extend the data lower in frequency to the fundamental of the PanDox system (model JC-200 with 0.96 MHz, 200 mm diameter, fixed focus source, Haifu Technology Company, Chongqing, China) and to numerically check for evidence of trapped gas or other strong path aberrations. Fit functions with R^2 values above 0.88 were retained as an automated analytical means of excluding aberrant measurements. Data failing this criterion reliably showed acute spectral features that suggested strong internal scattering which could be explainable by entrapped gas rather than any configuration of aqueous/fibrous tissue.

2.5 | Caliper nearfield simulations

Ultrasonic measurements of acoustic properties are often performed in the acoustic far field of the transducers employed[38,41] by introducing water or agar standoffs between the sample and transducer faces. In the current study, the samples were placed in direct contact with the transducer faces in order to keep the device more compact and easier to deploy in the hospital pathology lab where measurements were made. This configuration therefore placed the samples in the transducer nearfield. With the aim of quantifying what errors may therefore be encountered, the behavior of the transmit-receive measurement system was simulated numerically.

The transmit and receive transducers were modelled as circular baffled pistons with equal radii. The pressure field produced by the transmitter was evaluated in the frequency domain using a scaled version of the frequency-domain Rayleigh integral,[42] with leading terms irrelevant to the frequency dependence of the results omitted:

TABLE 1 Material parameters used in nearfield simulations.

Medium	c (m/s)	α (np/cm)[d]
Water, 37.0 C	1524	0
Pancreas, normal[a]	1550	$0.067\, f^{1.51}$
Liver tumour[b]	1568	$0.100\, f^{1.47}$
Generic tissue	1540	$0.060\, f^{1.00}$
Fat-like phantom[c]	1469	$0.035\, f^{1.90}$

[a]Based on preliminary results from this study.
[b]Ref. 33.
[c]Unpublished data.
[d]Frequency in MHz.

$$g(x,z) = \iint v(x_s, y_s) R^{-1} e^{ikR} e^{-\alpha R} dx_s dy_s \quad (4)$$

where x and z are lateral and axial field coordinates, respectively, $v(x_s, y_s)$ is the normal velocity on the surface at $z_s = 0$, $k = 2\pi f/c = \omega/c$ is the acoustic wavenumber, α is attenuation, and $R = \sqrt{(x_s - x)^2 + (y_s - y)^2 + z^2}$ is the slant range between each point on the source and each field computation location. Taking the velocity distribution to be uniformly unity makes Equation (4) an integration over free space Green's functions in an attenuating medium. The field points (x, z) were computed on the face of an equally sized circular piston parallel and co-axial to the source, noting that the axisymmetric nature of the field does not require additional computations for $y \neq 0$.

Calculations were performed for the cases listed in Table 1 and consisted of a 37°C, lossless water reference case used for calculation of attenuation and sound speed in combination with simulations performed in materials emulating tissue and phantom values. Spatially integrated values in water (p_{water}) and tissue/phantom materials (p_{mat}) were then used to estimate speed and attenuation at each source-receiver separation distance $z = h$:

$$\alpha_{mat}(f,z) = \ln\left(\left|g_{water}(f,z)/g_{mat}(f,z)\right|\right)/h \quad (5)$$

$$c_{mat}(f,z) = \left({}^{1}/_{c_{water}} - \varphi\left(g_{water}(f,z)/g_{mat}(f,z)\right)/\omega h\right)^{-1} \quad (6)$$

where $\varphi(\cdot)$ indicates the unwrapped phase angle of the water and material complex spectra.

The availability of this model allows for sample-specific correction for diffraction effects, if warranted. Specifically, the above calculations can be used to define a correction factor γ between the calliper-generated estimates and the actual material parameters:

$$\gamma(f,z) = \alpha_{mat}(f,z)/\alpha_{calliper}(f,z) \quad (7)$$

So that the diffraction-corrected measurement is:

$$\alpha_{calliper,diffcorr}(f,z) = \gamma(f,z)\,\alpha_{calliper,meas}(f,z) \quad (8)$$

2.6 | Validation experiment

A series of tissue phantom experiments was performed to validate the proposed methods. An agar-based phantom seeded with silicone carbide and aluminum oxide particles was chosen for its soft tissue-representative speed, attenuation, and scattering properties.[43] Samples were prepared by pouring into a single cylindrical mold and subsequently cutting the cured cylinder into three disks of thickness ranging from 14 – 21 mm, which were typical of the range encountered with the human pancreatic samples.

The samples were first interrogated with a 'long path' configuration shown in Figure 1B. This configuration consisted of a 12.7 mm diameter, 2.25 MHz center frequency unfocused transducer (Panametrics V306) used as a source, and a coaxially-aligned needle hydrophone (200 μm, Precision Acoustics, Dorchester, UK) placed 18 cm downrange. The use of a long water path between the source and the sample was intended to reduce incident field complexity, and the use of a needle hydrophone was intended to minimize receiver spatial integration. In the absence of any sample, a planar scan was performed with the hydrophone at a distance of 15 cm from the source to confirm the smoothness of the pressure amplitude and phase where the samples would subsequently be placed. For each sample, through-transmission data were collected at three independent sites. Caliper and 'long path' data were processed using the expressions in Section 2.4.

2.7 | Therapeutic ultrasound simulations

The impact of the measured pancreas properties on ultrasound mediated heating was assessed using a combination of linear and nonlinear finite element calculations based on the operation of the JC-200 clinical HIFU system employed for targeted drug delivery[26] and ablation[44] studies.

For assessments of mild hyperthermia, a clinically validated planning model was utilized,[27] having been recently modified for examining technical challenges in the treatment of pancreatic tumours.[45] Briefly, a three-dimensional acoustic model (Figure 2A) was constructed in PZFlex (v2015, OnScale, Redwood City, CA) based on segmented contrast CT image data from one patient, and the linearly propagating pressure field resulting from sonication with a 0.96 MHz, 200-mm diameter, 170-mm radius of curvature source was calculated. For the relatively low powers (30–50 W) and resulting focal pressures used for mild hyperthermia, nonlinear contributions are minimal and were neglected. Therefore, the linearly calculated pressures were used to determine heat generation terms from:

$$\dot{q} = 2\alpha I_{pa} \tag{9}$$

$$I_{pa} = \frac{1}{\rho c \tau_p} \int_{t=0}^{\tau} p^2 dt \tag{10}$$

where the intensity I_{pa} is calculated over the record time τ containing a single pulse of duration τ_p. Here, the attenuation is taken at the fundamental frequency of the HIFU system (0.96 MHz). The heat generation terms in Equation (9) were then applied to a bioheat transfer[46] finite model calculation in PZFlex, where temperature elevations were found for a 20-ms drive pulse corresponding to the shortest employed with the clinical system. The resulting temperature fields were used to simulate moving beam hyperthermia in an elliptical target volume with PDAC properties using procedures described previously.[45] The final form of the simulation is a volumetric temperature history from which cumulative metrics were computed to describe the median temperature (T_{50}) as well as the temperature exceeded in 10 and 90% of the treatment volume (T_{10}, T_{90}, respectively).

To simulate thermal ablation treatments where nonlinear contributions to heating from harmonic absorption are expected, the JC-200 source model was driven with an input power of 300 W in a nonlinear formulation of PZFlex utilizing a simplified axisymmetric layered tissue geometry (Figure 2B). The use of an axisymmetric model enabled the calculations to run with a mesh sufficient for capturing high frequency harmonics on existing computational hardware in a manageable time frame. Although clearly lacking the spatial complexity of the linear 3D model, the emphasis here was on the impact of local tissue properties which could be captured for this fixed (rather than scanning) beam scenario. Heating terms were calculated using frequency-integrated intensities and attenuation power law fits up to the 6th harmonic, where the mesh density of 14 μm was confirmed to be adequate through evaluation of convergence, and beyond which the contributions to heating were less than 1%. The property values used for all therapeutic simulations are listed in Table 2.

Finally, for higher power drive conditions required for boiling and intrinsic threshold histotripsy, axisymmetric pressure and heating rate calculations were carried out using the HIFUBeam[47] nonlinear ultrasound simulation code. Here, the source and tissue configurations were the same as used for thermal ablation simulations, with the exception that the pancreas and PDAC structures were implemented as planar layers defined by the outer envelopes of the elliptical shapes in Figure 2B (20 mm PDAC tumor thickness within a 30 mm thick pancreas layer). These simulations were intended to assess changes in required input power to reach a desired pressure as the pancreas ultrasonic properties were varied. As these models represent all materials as fluids, they do not include shear stiffness effects on probability of cavitation or bubble growth,[48] although the former appears to be minimally sensitive to background elasticity.[49]

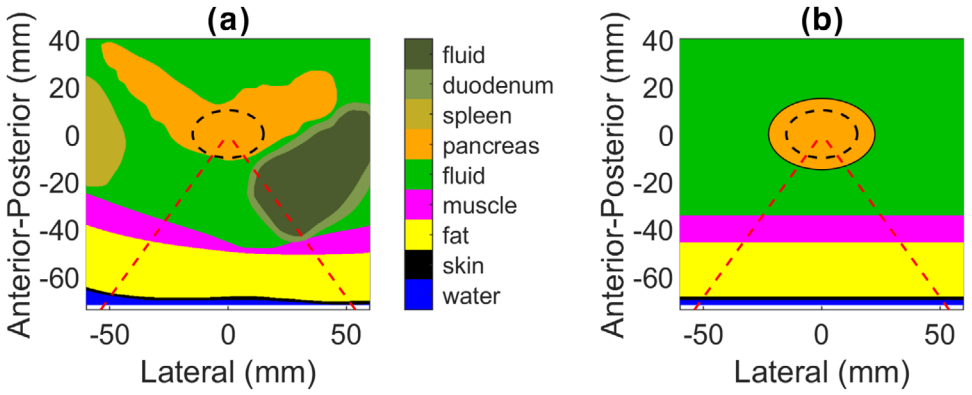

FIGURE 2 Model geometries for simulation of ultrasonic fields and resulting heat generation. (A) Central slice through the 3-D linear model. In this model, the spleen and duodenum were given properties of the fluid background for simplicity. (B) Axisymmetric nonlinear model. Red dashed lines indicate the outer 'cone' of the FUS field, and the PDAC target is outlined in dashed black.

TABLE 2 Properties used for acoustic and thermal simulations.

Tissue	Density (kg/m3)	Sound Speed (m/s)	Attenuation (np/cm)	B/A (–)	Thermal Conductivity (W/m/°C)	Specific Heat (J/kg/°C)	Perfusion (kg/s/m^3)
Pancreas							
Literature, Normal	1087[50]	1591[29]	0.091 $f^{1.13}$[30,31]	8.0[b]	0.458[51,52]	3188[51]	14.9[53–57]
Literature, Tumour	1087[50]	1591[29]	0.091 $f^{1.13}$[30,31]	8.0[b]	0.478[52]	3188[51]	5.2[53–57]
Human, Normal	1087[50]	1547.8[a]	0.074 $f^{1.42}$[a]	8.0[b]	0.458[51,52]	3188[51]	14.9[53–57]
Human, PDAC	1087[50]	1546.4[a]	0.060 $f^{1.65}$[a]	8.0[b]	0.478[52]	3188[51]	5.2[53–57]
Abdominal muscle	1050[58]	1547[58]	0.59 $f^{1.53}$[59–61]	7.8[62]	0.55[63]	3524[63]	0.48[63]
Abdominal fat	950[58]	1478[58]	0.59 $f^{1.53}$[59–61]	9.96[64,65]	0.19[63]	2353[63]	0.56[63]
Skin	1120[58]	1613[58]	1.57 $f^{1.00}$[58]	7.87[66]	0.40[67]	3391[50]	0.00

[a]This study.
[b]Assumed value in the absence of available data.

TABLE 3 Material parameter estimation results.

Medium	Sound speed			Attenuation		
	Actual (m/s)	Calliper (m/s)	Error[a] (%)	Actual (np/cm)	Caliper (np/cm)	Error[a] (%)
Pancreas	1550.0	1550.0	3e-3	$0.067\ f^{1.51}$	$0.063\ f^{1.54}$	2.9
Liver tumour	1568.0	1568.1	5e-3	$0.100\ f^{1.47}$	$0.092\ f^{1.52}$	3.6
Generic tissue	1540.0	1540.0	2e-3	$0.060\ f^{1.00}$	$0.056\ f^{1.03}$	3.7
Phantom	1469.0	1469.0	6e-4	$0.035\ f^{1.90}$	$0.037\ f^{1.66}$	2.2

[a]Error is averaged for sample thicknesses between 10 and 20 mm.

3 | RESULTS

3.1 | Caliper nearfield simulations

Simulated examples of caliper attenuation and sound speed estimation errors are summarized in Table 3 and shown in Figure 3 for the media listed in Table 1. For sample thicknesses in the 10–20 mm range, where most measurements in this study were performed, the attenuation estimation error ranges from 4.4–1.9% for the human pancreas case and is consistently biased below the actual values. Sound speed errors were much lower and appear to be negligible.

Similar outcomes were seen across the simulated tissues in Table 3. For the pancreas, liver, and generic tissue cases, the effect of the nearfield caliper measurements is to slightly elevate the frequency exponent and slightly decrement the attenuation coefficient. The trend is reversed for the 'phantom' case, whose sound speed is more indicative of fatty tissue. Although all the errors are small, suggesting that "nearfield effects" are limited in this configuration, it was judged preferable to remove the

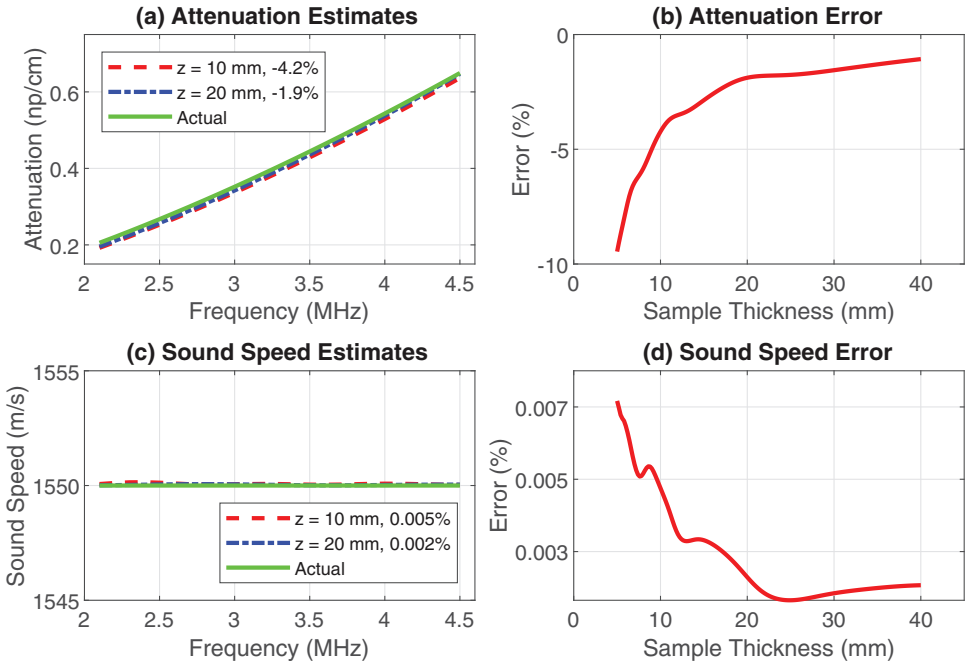

FIGURE 3 Attenuation and sound speed estimates and errors in a homogeneous medium mimicking normal human pancreas. (A) Attenuation estimates as a function of frequency for two tissue thicknesses. Frequency averaged estimation error (B) as a function of sample thickness, where a negative value means that the estimated attenuation was lower than the actual value. (C) Sound speed estimates as a function of frequency for the thicknesses in (A), and corresponding estimation errors (D). Legend values in (A) and (C) are root-mean-square errors between actual and estimated attenuation over the full frequency range.

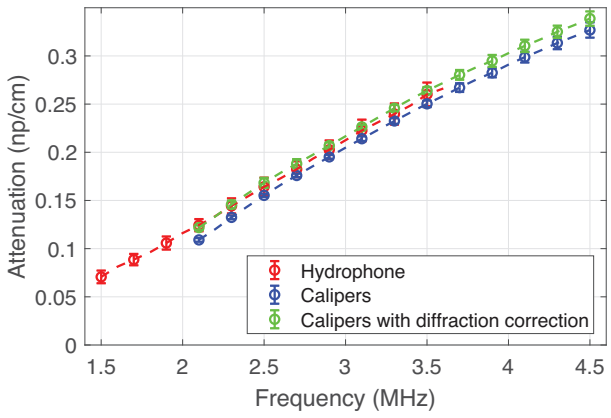

FIGURE 4 Tissue phantom attenuation estimates. Dashed lines and open circles indicate mean values ($N = 9$), while error bars show ± 1 standard deviation. The hydrophone and caliper data sets covered different transducer frequency ranges (see Sections 2.2 and 2.6).

biasing errors seen here by using the correction process described in Section 2.5.

3.2 | Validation experiment

Results of the validation experiment are shown in Figure 4, where the attenuation in a tissue mimicking phantom is displayed as a function of frequency for 'long path' and calliper-based measurements. The root-mean-square differences between measurement types were found from:

$$\epsilon = rms\left(1 - \alpha(f)_{caliper}/\alpha(f)_{longpath}\right) \quad (11)$$

and were 6.7% with processing as described in Section 2.4, reducing to 2.4% with a diffraction correction using the measured sound speed. Sound speeds (mean ± standard deviation, $N = 9$) were 1527.8 ± 1.9 and 1524.0 ± 1.5 m/s for the long path and calliper measurements, respectively, corresponding to a mean difference of 0.25%. These results serve to validate the proposed methods for calliper measurement and diffraction correction.

3.3 | Patient specimen information

A total of 23 surgical specimens were available for this study (Table S-1), of which 20 contained pancreas tissue initially thought to be suitable for ultrasound measurements. The mean patient age was 67 years and mean BMI (Body Mass Index) was 26.23 kg/m^2, consistent with clinical experience and published data on characteristics of the average patient undergoing resection for pancreatic cancer.[68] The specimens had a variety of background pathologies including PDAC, Neuroendocrine tumors, PanIN (pancreatic intra-epithelial

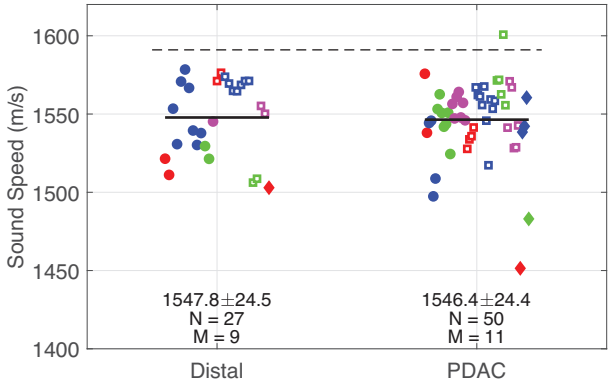

FIGURE 5 Pancreatic tissue sound speed estimates for 'Distal' and 'PDAC' tissue groups. Within each tissue group, symbols indicate individual patients, where colors and shapes were changed for ease of visualization. Solid horizontal lines indicate group means, displayed numerically at the bottom of the plot along with the standard deviation, number of measurements (N), and number of patients (M). The dashed black horizontal line is the literature value for ovine pancreas from Ref. 20.

neoplasia) and IPMN (Intraductal papillary mucinous neoplasm). However, the final pathologist reports classified 16 of the tumors as PDAC. Of these, two were not adequate for ultrasound data collection due to their small size and irregular geometry, and data were not successfully collected due to operator error in two other cases. Data from the small remainder of non-PDAC tumor cases did not meet the post-processing acceptance criteria, and there were no specimens deemed 'normal'. Results are therefore presented in two tissue groups: 'PDAC'—consisting solely of confirmed PDAC tumor tissue, and 'Distal'—consisting of tissue at least 1 cm from the tumor periphery and having no visible or tactile pathology.

As expected for surgically resectable PDAC, most tumors were located in the head and ampulla and were at an early T stage (maximum diameter less than 4 cm.) Between 2 and 15 measurements were made per specimen depending primarily on the quantity of available tissue, with the calipers moved to a new location for each measurement. Across the full data set, the mean and median tissue thicknesses interrogated by the calipers were 15.3 mm and 12.1 mm, respectively, spanning a full range of 5.4–65.9 mm.

3.4 | Sound speed

Sound speed data averaged over the 2.1–4.5 MHz analysis band are shown in Figure 5. Group mean values were within 1.4 m/s of each other, without a statistically significant difference. All but one of the sample values was below the lone literature report[29] shown with the dashed black line. A notably low departure was observed in the 'PDAC' group for a sample designated by the examining pathologist and visibly confirmable as 'fatty'. This sample had a sound speed of 1451.4 m/s.

3.5 | Attenuation

Attenuation coefficients and frequency exponents are shown in Figure 6. Visibly there is much greater spread in the attenuation data as quantified by mean-normalized standard deviations: ~1.6% for sound speed and 43.9% for attenuation coefficient in the PDAC group. The effect of diffraction correction (Figure 6B,D) is to raise the attenuation coefficient by 10.0–13.9% for the Distal and PDAC groups, but the majority of the data points remain below the range of the prior literature. There was no statistical significance between the tissue groups.

In contrast to the attenuation coefficients, frequency exponents decreased after diffraction correction, again consistent with the results in Sections 3.1 and 3.2. PDAC tissues have higher exponents, and the trend is for the present study values to generally exceed those in the pancreas literature.

Fitting a power law for each of the three data groups after diffraction correction yields the summary results shown in Figure 7 and listed in Table 2. Note that at 1 MHz, each power law fit will yield the attenuation coefficient value, so the low frequency fit projections are consistent with the human data that was characterized by lower attenuation coefficients than in the literature. All data fits had R^2 values exceeding 0.998. Again, the human data have lower attenuation coefficients and higher frequency exponents than the literature values.

The two prior pancreas studies have notably divergent trends, with data from the present study most closely resembling the results from Ref. 31 The literature average ($0.091\ f^{1.13}$) yields an attenuation coefficient substantially larger and a frequency exponent substantially smaller than the values from the present study. These differences have important implications for ultrasound therapies, as discussed in the next section.

3.6 | Acoustic and thermal simulations

Acoustic and thermal simulations were carried out using 'Distal' group properties to represent 'normal' pancreatic tissue, and 'PDAC' group properties for the tumor target. Results of mild hyperthermia simulations are shown in Figure 8, where the HIFU system input power was set with the goal of reaching a median temperature elevation of 41.0°C in the target volume and under the assumption that literature values were correct (taken here as sound speed from ref. 29 and the mean attenuation of Refs. 30, 31). Temperature elevations

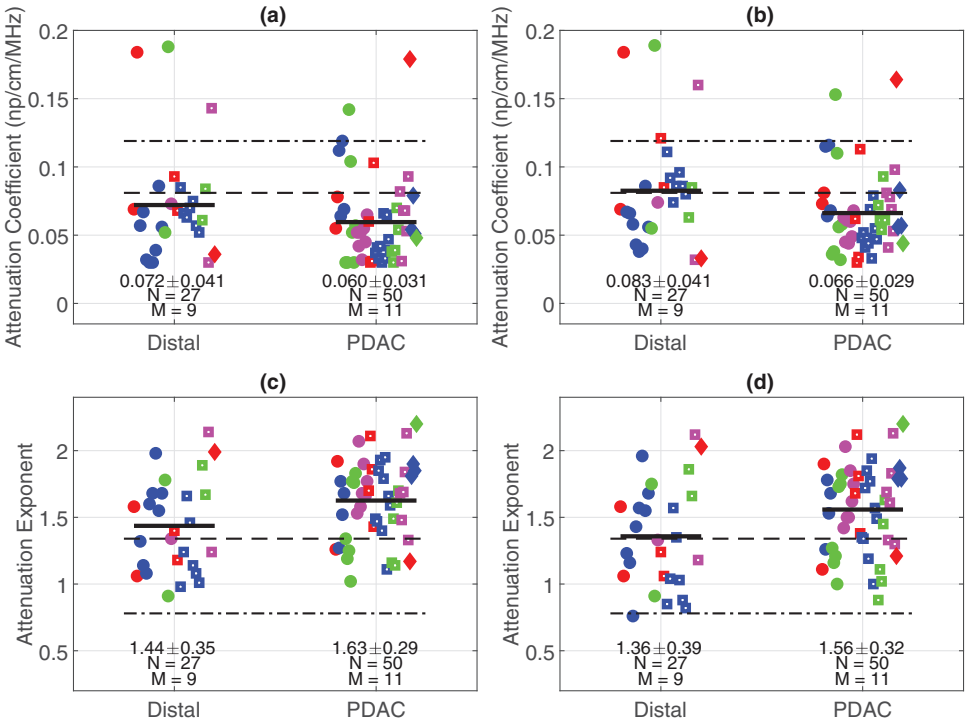

FIGURE 6 Pancreatic tissue attenuation coefficient (A, B) and power law frequency exponent (C,D) estimates for 'Distal' and 'PDAC' tissue groups processed without (A,C) and with (B,D) diffraction correction. Within each tissue group, symbols indicate individual patients, where colors and shapes were changed for ease of visualization. Solid black lines indicate group means, displayed numerically at the bottom of the plot along with the standard deviation, number of measurements (N), and number of patients (M). Literature values are shown in patterned lines: -. Refs. 30, 31.

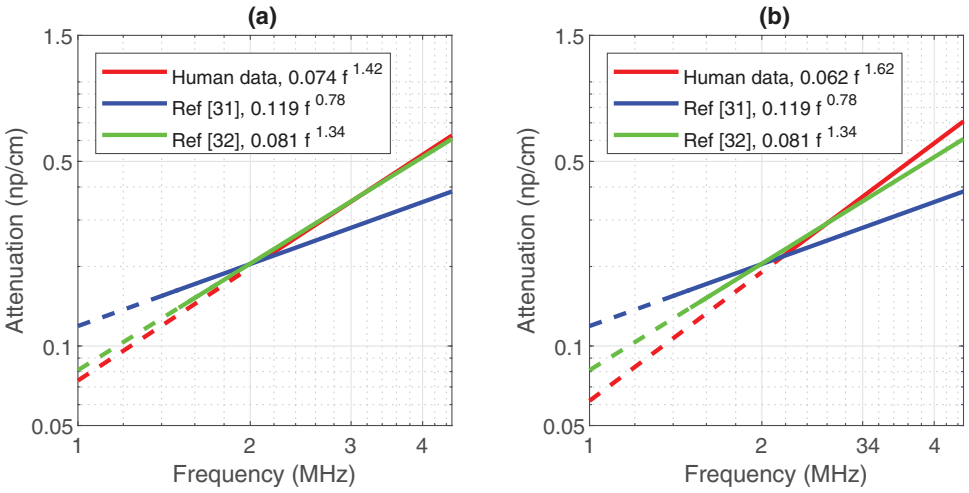

FIGURE 7 Pancreatic tissue attenuation frequency dependencies for (A) 'Distal' and (B) 'PDAC' tissue groups, shown with available literature values. Solid lines are in the measurement range of each study, and dashed lines are extensions using the power law fits down to 1.0 MHz. Results are displayed in log-log format to improve visualization at lower frequencies. Legend entries include power law fits (np/cm).

after a single 20-ms ultrasound pulse (Figure 8A) show a weaker effect with the human properties than with the literature, as expected from the lower attenuation/absorption at the drive frequency of 0.96 MHz. The variability in the human PDAC data set is evident in the range of elevations when assuming human properties within one standard deviation of the mean, and the "+ std" case is nearly equivalent to the literature mean. Peak temperatures occur ~2.5 mm short of the geometric HIFU focus because of refraction in the tissue path.

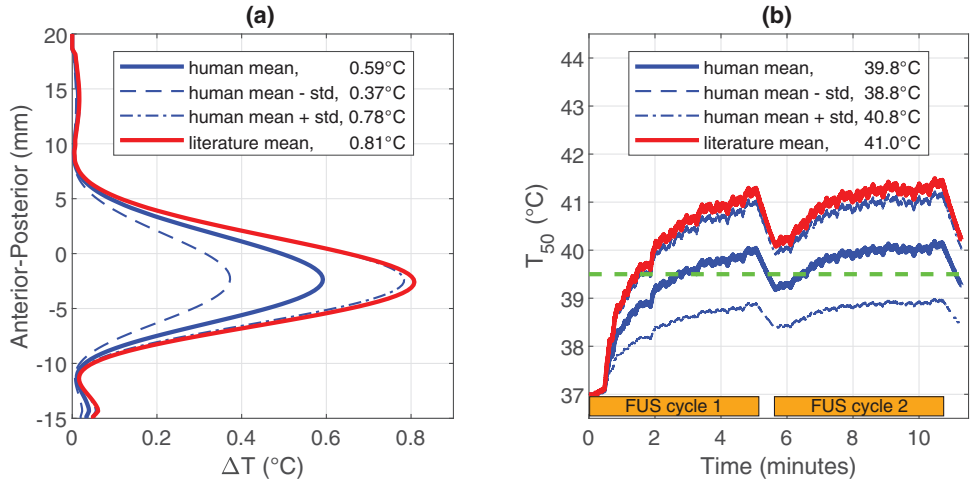

FIGURE 8 Linear 3-D simulations of ultrasound-mediated mild hyperthermia. (A) Anterior-posterior temperature elevation along the lateral centerline of the model after a single 20 ms exposure, with peak values in the legend. (B) T50 histories over two treatment cycles indicated by orange bars. Cycle 2 mean T_{50} values are listed in the legend, and the dashed green line indicates the threshold for drug release from ThermoDox®. This figure is an update to Figure 7 of Ref. 45 now using the full pancreas data set with diffraction-corrected attenuation. Literature mean refers to the mean of Refs. 30, 31 for attenuation and using sound speed from Ref. 29.

These trends translate directly to the median temperatures in the treatment volume after two cycles of moving beam hyperthermia as shown in Figure 8B. While the literature-based simulation reaches the target temperature of 41.0°C, the human mean simulation has a cycle-2 mean T_{50} of 39.8°C, which is just above the ThermoDox® release threshold (39.5°C). Therefore, assumption of literature mean values in these simulations could result in conditions that are borderline sufficient for drug release. The range of outcomes resulting from a single standard deviation of the human data span minimal ("- std") to ideal ("+ std") drug release conditions.

Results from the nonlinear heating simulations show a more nuanced picture. The spatial peak pressure spectra in Figure 9A show strong harmonic generation, as expected. The higher harmonic levels in the human set suggest that nonlinear generation occurs at the focus rather than in the path, since the human pancreas attenuation of the fundamental is lower and yields a higher pressure at the target. The spectrum data are cut off at 6 MHz because for the prescribed drive power of 300 W, harmonics at higher frequencies contribute less than 1% to the power deposition ($\dot{q}$) (Figure 9B) at any spatial location.

The power deposition spectra in Figure 9B show the human data to have a weaker fundamental contribution to heating and a stronger harmonic contribution, which in turn implies a physically narrower heat deposition pattern. This is verified in the thermal contours (Figure 9C) calculated at the end of the ultrasound exposure time. While both property sets yield similar peak temperatures (82.1 vs. 81.2°C, respectively for human and literature), the human data give a substantially smaller 60°C spot volume (2.2 vs. 3.7 mm^3, respectively). This suggests that lesion volumes would be smaller than expected if taking the literature mean property values to be correct, and the discrepancies could be greater if higher system drive powers were used. Note that refraction shifting of the heating pattern in these examples is weaker than in the 3D models because of the reduced path complexity in the nonlinear calculations.

Results of the higher power simulations related to histotripsy are shown in Figure 10, where the differential effects of changing tissue properties are muted compared with earlier hyperthermia examples. In Figure 10(A/B) the source drive power was set to provide pressures that were appropriate for histotripsy via boiling or shock front scattering, while the power specified for Figure 10(C) was intended to provide a peak negative pressure capable of intrinsic threshold histotripsy.

The change from literature to human average properties slightly (~14.7%) reduced the peak positive pressure and had no meaningful impact (<1%) on the size of the peak negative pressure for either of the drive powers evaluated. The fields appear to be saturated, as the driving pressure ratio between 10(A) and 10(C) was 2.2, but the peak pressure ratio was 1.4 for both tissue sets. In Figure 10(B) the peak heating rate at 1 kW was 23.4% lower with human properties than with the literature values – closer to the literature result than in the linear heating example (34.1%) -and illustrative of the impact of the higher attenuation exponent in the human data set. This is also the cause of the suppressed diffraction shock peak[47] 5 mm proximal of the geometric focus in Figure 10(C). Overall, it appears that the effects of attenuation changes from literature to human (stronger expected shock absorption) may have been partially offset by the changes in sound speed (weaker nonlinear waveform enhancement[69]) for this particular long-focus source geometry and propagation

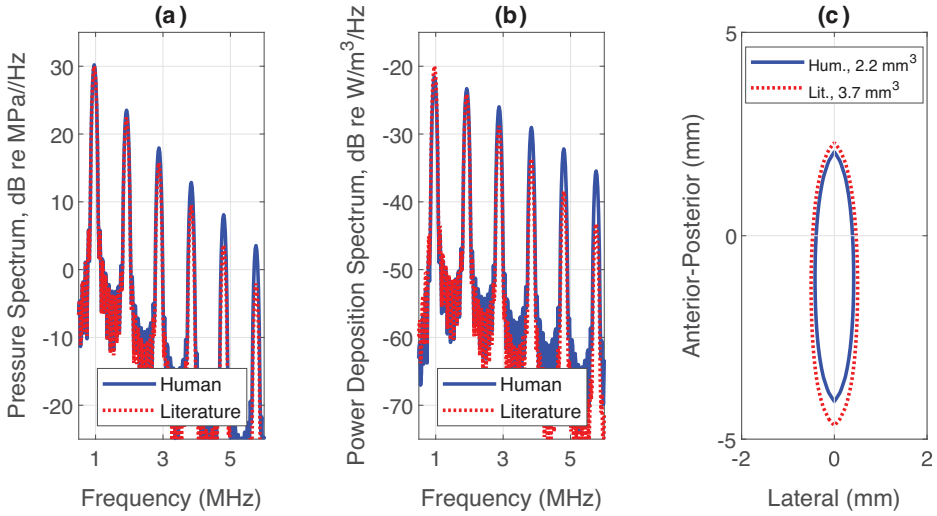

FIGURE 9 Nonlinear heating simulations using human and literature mean acoustic properties. (A) Power spectral density of spatial peak pressure. (B) Power deposition spectrum ($\dot{q}$) corresponding to the pressures in (A). (C) Temperature contours at 60°C after 300 W exposure, with spot volumes noted in the legend. Literature mean refers to the mean of Refs. 30, 31 for attenuation and using sound speed from Ref. 29.

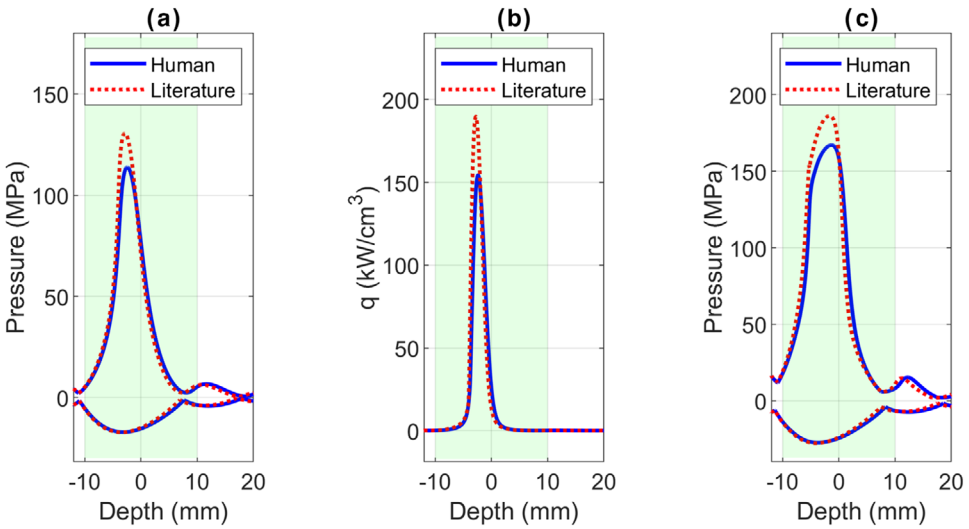

FIGURE 10 Nonlinear simulations using human and literature mean acoustic properties. (A) Envelopes of on-axis peak pressures for 1.0 kW source drive power. (B) Power deposition corresponding to (A). (C) Envelopes of on-axis peak pressures for 5.0 kW source drive power. The displayed depth range bounds the pancreas, and green shading bounds the tumor. Depths are shown relative to the HIFU geometric focus. Literature mean refers to the mean of Refs. 30, 31 for attenuation and using sound speed from Ref. 29.

environment. This is in contrast to the thermal therapies, whose results were predominantly modified by attenuation. Further studies are needed to understand the impacts over a broader range of target depths, tumor sizes, and source configurations.

4 | DISCUSSION

This study shows that the sound speeds and attenuation coefficients in pathological human pancreata were lower than data available in the literature for large animal samples (Figures 5–7), highlighting the need for well-documented and validated measurements on human tissues to be targeted in candidate therapies. The impacts on ultrasound-mediated heating varied by application, with the lower attenuation coefficients leading to reduced heating rates in mild-hyperthermia simulations near 1 MHz (Figure 8) and the higher frequency exponents leading to reduced thermal spot sizes in nonlinear ablation simulations (Figure 9) where heat deposition is strongly impacted by harmonic absorption.

There are a great many ways in which methodological differences and measurement errors can contribute to differences in reported tissue property values.[40] The processing, validation, and diffraction correction methodologies employed in this study (Figure 4) are intended to give the most accurate results possible with a physically compact system that is suitable for data collection in a busy hospital laboratory environment.

The lone pancreas sound speed data in the literature[29] were collected at 100 MHz for ovine samples examined at 23–26°C. Sample thicknesses were on the order of 0.1 mm, although it was separately reported for this technique[70] that thickness could only be measured within 10%, and by using such thin specimens, the heterogenous nature of the tissue may not be fully appreciated.[71] In the present study, measurements were conducted at physiologic temperature and with thickness measured to within less than 1% of the smallest samples collected (5.4 mm).

Two prior literature sources have reported pancreas attenuation data. In the first,[30] the incident field was transmitted through bovine samples at 1.4 MHz and its 3rd, 5th and 7th harmonics in turn as part of a radiation force-based measurement system. There was no report of the spectral purity of the transmissions, which is important since the radiation force measurement integrates all spectral components and could be skewed by inadvertent harmonic generation. The reported data fit of 0.119 $f^{0.78}$ (np/cm) was notable for its unusually small frequency exponent relative to the soft tissue literature. There was no report of methodological validation, and measurements were made at room temperature (24°C).

In the second source for pancreas data,[31] the field incident on the porcine tissue samples was swept over a broad range of frequencies, allowing analysis in 0.1 MHz bands. Tissues were placed in a sealed bag and hung between transducers, but it was unclear what thickness was measured or to what accuracy. The process for including data in group averages was subjective and based on the user's interpretation of consistency with the set as a whole. By contrast, the present study used a user-independent calculation to assess measurement validity, and thickness measurement was made directly on the sample during ultrasound exposure. That report also featured data for one human pancreas whilst noting that it was very difficult to determine sample thickness, and the results are therefore not thought to be reliable.

The existing literature values were taken on tissues within 3–5 h post-mortem. Our results were collected within a similar timeframe and therefore cannot account for the differences in acoustic values. Studies of short-term post-mortem changes in acoustic properties suggest a minimal impact[67] and therefore we would expect our results to reflect in vivo measurements. However, there will always be uncertainty with ex vivo data without direct validation on human tissues in situ.

The differences between the human and large animal data may perhaps be explained by a difference in composition between the human organs in our samples and that of the healthy mammalian organs. A high-fat diet is a known risk factor for pancreatitis and pancreatic cancer, and pancreatitis was reported in the background tissue of several organs in our study. We observed a lower sound speed in one organ noted to have a particularly fatty histological appearance and it is certainly possible that all our human specimens had a higher fat content than that of the animal samples in the existing literature. Hydroxyproline concentration, as a surrogate marker for tissue protein content, has been measured in other studies involving mammalian tissues and no statistically significant relationship with frequency-dependent ultrasonic attenuation coefficient was observed.[30] It may be that the type of protein, rather than total protein content, is more important as relative proportions of globular and structural proteins may correspond to ultrasonic propagation properties.[72]

Within our data we found no significant difference in speed or attenuation between PDAC and Distal tissue groups (Figures 5 and 6). This is consistent with work comparing distinct pancreatic regions, where similar sound speeds were measured in soft exocrine pancreas and firmer Islets of Langerhans.[29] Future work should include quantification of total protein, collagen and fat content to accompany acoustic property data collection.

The attenuation data in our study showed substantial variation (Figure 6), with mean-normalized standard deviations on the order of 50%, which is higher than reported in a recent study on liver tumor and peritumoral tissue[41] showing mean ranges of 30%–44%. This, along with the trend toward higher attenuation frequency exponents in the pancreas data sets may be attributable to the relatively high morphological complexity in comparison to liver. There may be a comparable effect when comparing different sections of kidney.[50] but more effort is needed to understand the observed trends. The limited sample size in this study may also have contributed to the noted variability, although a high degree of variation was also observed within individual patients.

The large range in measured attenuations raises a question of the data's value for treatment planning. Certainly, patient specific in vivo estimates would be best, but in their absence, an awareness of the property averages and ranges could still allow for justifiable scenario planning, particularly for thermal therapies. Clinical experience[26] and related simulations[27,45] have shown that mild hyperthermia of tumor target volumes is relatively tolerant of local tissue property variability. This is thought to be because the heat deposition at any one sonication location is not solely responsible for sustained heating of that location—instead heating is provided over most of the exposure time by diffusion from neighboring regions. In a spatial and temporal average sense, the importance of local tissue properties

tends to be reduced for this type of therapy, but the large range of measured attenuation values suggests a greater need for temperature monitoring in pancreas treatments than for those in the liver.[26] By contrast, ablation therapies that treat a volume through a series of fixed position sonications may be more sensitive to the local tissue properties. However, the efficacy of these methods can be more readily tracked with existing real time modalities such as B-mode (via echo enhancement) or MR thermometry.

The diffraction correction applied during data processing adds negligible time to the computations and appears to yield improved results in a homogeneous tissue phantom (Figure 4). However, potential complications of making measurements in the transducer nearfield remain. Refraction, diffraction and scattering effects in real, complex tissue structures could influence any measurement whether in the nearfield or not, and every system leaves its 'fingerprint' on the collected and processed data.[40] The significance of tissue structure and application of diffraction (or other) corrections for tissue property measurements are the subjects of ongoing research.

As simulated in this study, mild hyperthermia relies primarily on the fundamental frequency for heating, and in the case of the JC200 clinical system, the attenuation differences at 0.96 MHz were considerable in comparison to the literature (Figure 7) and led to reduced heating with the human values. A different choice of fundamental frequency may show a weaker or stronger influence of tissue properties whether from our study or the literature. For example, at 5 MHz—a frequency relevant for endoluminal devices,[17] the attenuation values would project to 0.56 and 0.84 np/cm for the literature and human PDAC average data sets, respectively. The 50% higher human attenuation would enhance path and local absorption while reducing transmitted intensity to the targeted region. These effects may largely offset each other in a linear thermal scenario, leading to a net reduction of heat deposition rate 1-cm into the PDAC target of only 17% when using the human properties. For nonlinearly enhanced thermal ablation, the higher human data frequency exponent would likely counteract the linear trend above and lead to more pronounced and spatially concentrated heating from harmonic absorption at the target.

In contrast, pancreas ultrasonic properties had a relatively minor impact on pressure field generation for histotripsy, especially in the intrinsic threshold scenario. Even if this had not been the case, cavitation emissions generated by this class of techniques may provide the basis for treatment guidance[73,74] and safe ramping of drive powers to generate the desired effects.

The mild hyperthermia calculations in this study were motivated by concepts for ultrasound-mediated drug release from thermally sensitive liposomes, where temperature-related effects on the quantity of bioavailable drug and its distribution are of interest. As the temperature is lowered towards the liposome release threshold, lower amounts of bioavailable drug will become available, as was quantified in simulations and measurements of ultrasound mediated hyperthermia in a rabbit thigh model that considered perfusion, transvascular transport, and intracellular uptake.[75] Treatments suffering from incomplete drug release at lower temperatures may also lose therapeutic synergy from increases in perfusion and permeability of tumor vasculature[76] at 42°C.

In the case of overheating to higher temperatures, there is increased risk of vascular shutdown,[77] which would inhibit transport of free drug to the targeted cancer cells. These factors have motivated the development of MR-guided control algorithms which can provide highly precise and stable temperature control in targeted regions, as recently demonstrated in muscle tissue of a porcine model.[78] The degree to which such enhanced temperature control translates to improved therapeutic outcomes in the pancreas is currently unknown.

In the absence of available data, the high-power simulations employed for thermal and mechanical ablation all used a single assumed value for the parameter of nonlinearity. Future investigations of high power treatments should include measurements of this parameter for the targeted and peripheral tissues, and notably, the basic caliper design used in this study was originally intended for that purpose.[37]

Finally, the histotripsy simulations were presented to demonstrate limited examples of material property impacts, but these calculations certainly do not span the range of clinical possibilities. For example, boiling and intrinsic threshold histotripsy systems may operate at considerably different frequencies[7] than the 0.96 MHz value used here, and their vastly different pulse lengths may lead to distinct nonlinear pressure waveform shapes.[79] Moreover, the material assignments for each tissue were defined as homogeneous within planar layers, which is a convenient but restrictive approach, especially when the results may be sensitive to refraction in the propagation path. More detailed and accurate models are of interest across the fields of radiology and oncology with the aim of accurately representing real treatment scenarios.

5 | CONCLUSIONS

Ultrasonic characterization measurements on human pancreatic tissues were performed using validated experimental and post-processing procedures and indicated generally lower sound speeds and attenuation coefficients and higher power law exponents than the available large animal literature. In the resulting

simulations, the reduced attenuation coefficient led to substantially reduced ultrasound heating in a linear regime, the elevated frequency exponent led to a significantly reduced spot size for thermal ablation, but the combined effects of attenuation and sound speed changes for histotripsy-like conditions were relatively minor. Researchers should seek the best available data for target tissues in candidate therapies and should endeavor to collect the required data if little is available. This study may serve as a renewed warning of the risks that may be incurred if overly reliant on literature results, as well as of the variability in pancreas tissue attenuation that may make treatment planning in this complex organ particularly challenging.

ACKNOWLEDGMENTS

The authors wish to thank David Maldonado-Perez, Adam Appelbee, Callum Board, and Dr. Aniko Rendek at the John Radcliffe Hospital pathology laboratory for their time and effort in supporting data collection for this study. The authors further thank Dr. Luca Bau for helpful discussions and James Fisk for machining of parts for the ultrasonic callipers. This work was supported by the National Institute for Health Research (NIHR) Oxford Biomedical Research Centre (BRC). The views expressed are those of the author(s) and not necessarily those of the National Health Service, the National Institute for Health Research, or the Department of Health.

CONFLICT OF INTEREST STATEMENT

The authors have no conflicts to disclose.

REFERENCES

1. Sofuni A, Asai Y, Mukai S, Yamamoto K, Itoi T. High-intensity focused ultrasound therapy for pancreatic cancer. *J Med Ultrason*. 2022.
2. Ćwik G, Gierbliński IW. Errors and mistakes in the ultrasound diagnosis of the pancreas. *J Ultrason*. 2013;13(53):178-191.
3. e Silva LdLS, Fernandes MSdS, Lima EAd, Stefano JT, Oliveira CP, Jukemura J. Fatty Pancreas: disease or Finding? *Clinics*. 2021;76:e2439.
4. Xi M, Liu MZ, Li QQ, Cai L, Zhang L, Hu YH. Analysis of abdominal organ motion using four-dimensional CT. *Ai Zheng*. 2009;28(9):989-993.
5. Wu F, Wang ZB, Zhu H, et al. Feasibility of US-guided high-intensity focused ultrasound treatment in patients with advanced pancreatic cancer: initial experience. *Radiology*. 2005;236(3):1034-1040.
6. Hendricks-Wenger A, Sereno J, Gannon J, et al. Histotripsy ablation alters the tumor microenvironment and promotes immune system activation in a subcutaneous model of pancreatic cancer. *IEEE Trans Ultrason Ferroelectr Freq Control*. 2021;68(9):2987-3000.
7. Xu Z, Hall TL, Vlaisavljevich E, Lee FT. Histotripsy: the first non-invasive, non-ionizing, non-thermal ablation technique based on ultrasound. *Int J Hyperthermia*. 2021;38(1):561-575.
8. Khokhlova VA, Fowlkes JB, Roberts WW, et al. Histotripsy methods in mechanical disintegration of tissue: towards clinical applications. *Int J Hyperthermia*. 2015;31(2):145-162.
9. Erkan M, Hausmann S, Michalski CW, et al. The role of stroma in pancreatic cancer: diagnostic and therapeutic implications. *Nat Rev Gastroenterol Hepatol*. 2012;9(8):454-467.
10. Dimcevski G, Kotopoulis S, Bjanes T, et al. A human clinical trial using ultrasound and microbubbles to enhance gemcitabine treatment of inoperable pancreatic cancer. *J Controlled Release*. 2016;243:172-181.
11. Ranjan A, Jacobs GC, Woods DL, et al. Image-guided drug delivery with magnetic resonance guided high intensity focused ultrasound and temperature sensitive liposomes in a rabbit Vx2 tumor model. *J Control Release*. 2012;158(3):487-494.
12. Li T, Wang YN, Khokhlova TD, et al. Pulsed high-intensity focused ultrasound enhances delivery of doxorubicin in a preclinical model of pancreatic cancer. *Cancer Res*. 2015;75(18):3738-3746.
13. Villadolid J, Amin A. Immune checkpoint inhibitors in clinical practice: update on management of immune-related toxicities. *Transl Lung Cancer Res*. 2015;4(5):560-575.
14. Valkenburg KC, de Groot AE, Pienta KJ. Targeting the tumour stroma to improve cancer therapy. *Nat Rev Clin Oncol*. 2018;15(6):366-381.
15. Dromi S, Frenkel V, Luk A, et al. Pulsed-high intensity focused ultrasound and low temperature-sensitive liposomes for enhanced targeted drug delivery and antitumor effect. *Clin Cancer Res*. 2007;13(9):2722-2727.
16. Farr N, Wang YN, D'Andrea S, et al. Hyperthermia-enhanced targeted drug delivery using magnetic resonance-guided focussed ultrasound: a pre-clinical study in a genetic model of pancreatic cancer. *Int J Hyperthermia*. 2018;34(3):284-291.
17. *NCT02439593: Concurrent hyperthermia and chemoradiotherapy in LAPC: phase II study (HEATPAC)*. Accessed 03 August 2022, 2022. https://clinicaltrials.gov/ct2/show/NCT02439593
18. NCT04889742: Hyperthermia enhanced re-irradiation of loco-regional recurrent tumors (HETERERO), Accessed 03 August 2022, 2022. https://clinicaltrials.gov/ct2/show/NCT04889742
19. *NCT01786850: Magnetic Resonance-guided high-intensity focused ultrasound treatment of locally advanced pancreatic cancer*. Accessed 03 August 2022. https://clinicaltrials.gov/ct2/history/NCT01786850
20. *NCT05010226: Focused ultrasound for the treatment of pancreatic cancer – an international registry*. Accessed 03 August 2022. https://clinicaltrials.gov/ct2/show/NCT05010226
21. Frenkel V, Etherington A, Greene M, et al. Delivery of liposomal doxorubicin (Doxil) in a breast cancer tumor model: investigation of potential enhancement by pulsed-high intensity focused ultrasound exposure. *Acad Radiol*. 2006;13(4):469-479.
22. Staruch R, Chopra R, Hynynen K. Localised drug release using MRI-controlled focused ultrasound hyperthermia. *Int J Hyperthermia*. 2011;27(2):156-171.
23. Guillemin PC, Gui L, Lorton O, et al. Mild hyperthermia by MR-guided focused ultrasound in an ex vivo model of osteolytic bone tumour: optimization of the spatio-temporal control of the delivered temperature. *J Transl Med*. 2019;17(1):350.
24. Rieke V, Pauly K. MR thermometry. *J Magn Reson Imaging*. 2008;27(2):376-390.
25. Winter L, Oberacker E, Paul K, et al. Magnetic resonance thermometry: methodology, pitfalls and practical solutions. *Int J Hyperthermia*. 2016;32(1):63-75.
26. Lyon PC, Gray MD, Mannaris C, et al. Safety and feasibility of ultrasound-triggered targeted drug delivery of doxorubicin from thermosensitive liposomes in liver tumours (TARDOX): a single-centre, open-label, phase 1 trial. *Lancet Oncol*. 2018;19(8):1027-1039.
27. Gray MD, Lyon PC, Mannaris C, et al. Focused Ultrasound Hyperthermia for Targeted Drug Release from Thermosensitive Liposomes: results from a Phase I Trial. *Radiology*. 2019;291(1):232-238.

28. *NCT04852367: Targeted doxorubicin in pancreatic tumours (PanDox)*. Accessed 03 August 2022. https://clinicaltrials.gov/ct2/show/NCT04852367
29. Frizzell LA, Gindorf JD. Measurement of ultrasonic velocity in several biological tissues. *Ultrasound Med Biol*. 1981;7(4):385-387.
30. Segal L, O'Brien W, Frequency dependent ultrasonic attenuation coefficient assessment in fresh tissue. Ultrasonics Symposium; 1983.
31. Le Croisette D, Heyser R, Gammell P, Wilson R. *Final report: tissue identification by ultrasound*. Jet Propulsion Laboratory; 1978.
32. Adams MS, Scott SJ, Salgaonkar VA, Sommer G, Diederich CJ. Thermal therapy of pancreatic tumours using endoluminal ultrasound: parametric and patient-specific modelling. *Int J Hyperthermia*. 2016;32(2):97-111.
33. Nightingale K, Soo MS, Nightingale R, Trahey G. Acoustic radiation force impulse imaging: in vivo demonstration of clinical feasibility. *Ultrasound Med Biol*. 2002;28(2):227-235.
34. Bailey MR, Khokhlova VA, Sapozhnikov OA, Kargl SG, Crum LA. Physical mechanisms of the therapeutic effect of ultrasound - (A review). *Acoust Phys*. 2003;49(4):369-388.
35. Sarvazyan AP, Rudenko OV, Swanson SD, Fowlkes JB, Emelianov SY. Shear wave elasticity imaging: a new ultrasonic technology of medical diagnostics. *Ultrasound Med Biol*. 1998;24(9):1419-1435.
36. Canney MS, Khokhlova VA, Bessonova OV, Bailey MR, Crum LA. Shock-induced heating and millisecond boiling in gels and tissue due to high intensity focused ultrasound. *Ultrasound Med Biol*. 2010;36(2):250-267.
37. Zhang J, Dunn F. In vivo B/A determination in a mammalian organ. *J Acoust Soc Am*. 1987;81(5):1635-1637.
38. Zderic V, Keshavarzi A, Andrew MA, Vaezy S, Martin RW. Attenuation of porcine tissues in vivo after high-intensity ultrasound treatment. *Ultrasound Med Biol*. 2004;30(1):61-66.
39. Marczak W. Water as a standard in the measurements of speed of sound in liquids. *J Acoust Soc Am*. 1997;102(5):2776-2779.
40. Hill CR, Bamber JC, ter Haar GR. *Physical Principles of Medical Ultrasonics*. 2nd ed. John Wiley & Sons; 2004.
41. Barrere V, Sanchez M, Cambronero S, Dupre A, Rivoire M, Melodelima D. Evaluation of ultrasonic attenuation in primary and secondary human liver tumors and its potential effect on high-intensity focused ultrasound treatment. *Ultrasound Med Biol*. 2021;47(7):1761-1774.
42. Pierce AD. *Acoustics: An Introduction to its Physical Principles and Applications*. Acoustical Society of America; 1994. 1994 Edition ed.
43. Ramnarine KV, Anderson T, Hoskins PR. Construction and geometric stability of physiological flow rate wall-less stenosis phantoms. *Ultrasound Med Biol*. 2001;27(2):245-250.
44. Gillies MJ, Lyon PC, Wu F, et al. High-intensity focused ultrasonic ablation of sacral chordoma is feasible: a series of four cases and details of a national clinical trial. *Br J Neurosurg*. 2017;31(4):446-451.
45. Gray M, Spiers L, Coussios C. Effects of human tissue acoustic properties, abdominal wall shape, and respiratory motion on ultrasound-mediated hyperthermia for targeted drug delivery to pancreatic tumors. *Int J Hyperthermia*. 2022;39(1):918-934.
46. Pennes HH. Analysis of tissue and arterial blood temperatures in the resting human forearm. *J Appl Physiol*. 1948;1(2):93-122.
47. Yuldashev PV, Karzova MM, Kreider W, Rosnitskiy PB, Sapozhnikov OA, Khokhlova VA. "HIFU beam:" a simulator for predicting axially symmetric nonlinear acoustic fields generated by focused transducers in a layered medium. *IEEE Trans Ultrason Ferroelectr Freq Control*. 2021;68(9):2837-2852.
48. Vlaisavljevich E, Lin KW, Warnez MT, et al. Effects of tissue stiffness, ultrasound frequency, and pressure on histotripsy-induced cavitation bubble behavior. *Phys Med Biol*. 2015;60(6):2271-2292.
49. Vlaisavljevich E, Lin KW, Maxwell A, et al. Effects of ultrasound frequency and tissue stiffness on the histotripsy intrinsic threshold for cavitation. *Ultrasound Med Biol*. 2015;41(6):1651-1667.
50. Hasgall PA, DG F, et al. *IT'IS database for thermal and electromagnetic parameters of biological tissues*. Accessed 22 February 2022. www.itis.ethz.ch/database
51. Valvano JW, Cochran JR, Diller KR. Thermal-conductivity and diffusivity of biomaterials measured with self-heated thermistors. *Int J Thermophys*. 1985;6(3):301-311.
52. Bowman HF. Heat transfer and thermal dosimetry. *J Microw Power*. 1981;16(2):121-133.
53. Kandel S, Kloeters C, Meyer H, Hein P, Hilbig A, Rogalla P. Whole-organ perfusion of the pancreas using dynamic volume CT in patients with primary pancreas carcinoma: acquisition technique, post-processing and initial results. *Eur Radiol*. 2009;19(11):2641-2646.
54. Delrue L, Blanckaert P, Mertens D, Van Meerbeeck S, Ceelen W, Duyck P. Tissue perfusion in pathologies of the pancreas: assessment using 128-slice computed tomography. *Abdom Imaging*. 2012;37(4):595-601.
55. Klauss M, Stiller W, Fritz F, et al. Computed Tomography Perfusion Analysis of Pancreatic Carcinoma. *J Comput Assist Tomogr*. 2012;36(2):237-242.
56. Klauss M, Stiller W, Pahn G, et al. Dual-energy perfusion-CT of pancreatic adenocarcinoma. *Eur J Radiol*. 2013;82(2):208-214.
57. Li HO, Guo J, Sun C, et al. Assessment of pancreatic adenocarcinoma: use of low-dose whole pancreatic CT perfusion and individualized dual-energy CT scanning. *J Med Imaging Radiat Oncol*. 2015;59(5):590-598.
58. Mast TD, Hinkelman LM, Orr MJ, Waag RC. The effect of abdominal wall morphology on ultrasonic pulse distortion. Part II. Simulations. *J Acoust Soc Am*. 1998;104(6):3651-3664.
59. Siddiqi TA, Obrien WD, Meyer RA, Sullivan JM, Miodovnik M. Human in situ dosimetry - differential insertion loss during passage through abdominal wall and myometrium. *Ultrasound Med Biol*. 1992;18(8):681-689.
60. Hinkelman LM, Mast TD, Metlay LA, Waag RC. The effect of abdominal wall morphology on ultrasonic pulse distortion. Part I. Measurements. *J Acoust Soc Am*. 1998;104(6):3635-3649.
61. El-Brawany MA, Nassiri DK, ter Haar G, Shaw A, Rivens I, Lozhken K. Measurement of thermal and ultrasnic properties of some biological tissues. *J Med Eng Technol*. 2009;33(3):249-256.
62. Law WK, Frizzell LA, Dunn F. Determination of the nonlinearity parameter B/A of biological media. *Ultrasound Med Biol*. 1985;11(2):307-318.
63. Sekins K, Emery A. Thermal science for physical medicine. In: Lehmann J, ed. *Therapeutic Heat and Cold*. 3 ed. Willimans & Wilkins; 1982:70-132.
64. Sehgal CM, Bahn RC, Greenleaf JF. Measurement of the acoustic nonlinearity parameter B/A in human tissues by a thermodynamic method. *J Acoust Soc Am*. 1984;76(4):1023-1029.
65. Errabolu RL, Sehgal CM, Bahn RC, Greenleaf JF. Measurement of ultrasonic Nonlinear parameter in excised fat tissues. *Ultrasound Med Biol*. 1988;14(2):137-146.
66. Sun Y, Dong Y, Tong J, Tang Z, Ultrasonic Propagation Parameters in Human Tissues. Paper presented at: IEEE 1986 Ultrasonics Symposium; 17–19 Nov. 1986, 1986.
67. Duck F. *Physical Properties of Tissue: A Comprehensive Reference Book*. Academic Press; 1990.
68. Network NCI. *NHS treated cancer patients receiving major surgical resections*. Accessed 19 September 2022, http://www.ncin.org.uk/publications/data_briefings/major_resection 2022.
69. Bessonova OV, Khokhlova VA, Bailey MR, Canney MS, Crum LA. Focusing of high power ultrasound beams and limiting values of shock wave parameters. *Acoust Phys*. 2009;55(4-5):463-473.
70. Goss SA , O'Brien, WD Jr. Direct ultrasonic velocity measurements of mammalian collagen threads. *J Acoust Soc Am*. 1979;65(2):507-511.

71. Kolosov OV, Levin VM, Mayev RG, Senjushkina TA. The use of acoustic microscopy for biological tissue characterization. *Ultrasound Med Biol*. 1987;13(8):477-483.
72. Goss SA, Frizzell LA, Dunn F, Dines KA. Dependence of the ultrasonic properties of biological tissue on constituent proteins. *J Acoust Soc Am*. 1980;67(3):1041-1044.
73. Sukovich JR, Macoskey JJ, Lundt JE, Gerhardson TI, Hall TL, Xu Z. Real-Time Transcranial Histotripsy Treatment Localization and Mapping Using Acoustic Cavitation Emission Feedback. *IEEE Trans Ultrason Ferroelectr Freq Control*. 2020;67(6):1178-1191.
74. Bhargava A, Huang SL, McPherson DD, Bader KB. Assessment of bubble activity generated by histotripsy combined with echogenic liposomes. *Phys Med Biol*. 2022;67(21):13.
75. Gasselhuber A, Dreher MR, Partanen A, et al. Targeted drug delivery by high intensity focused ultrasound mediated hyperthermia combined with temperature-sensitive liposomes: computational modelling and preliminary in vivovalidation. *Int J Hyperthermia*. 2012;28(4):337-348.
76. Kong G, Braun RD, Dewhirst MW. Hyperthermia enables tumor-specific nanoparticle delivery: effect of particle size. *Cancer Res*. 2000;60(16):4440-4445.
77. Gasselhuber A, Dreher MR, Negussie A, Wood BJ, Rattay F, Haemmerich D. Mathematical spatio-temporal model of drug delivery from low temperature sensitive liposomes during radiofrequency tumour ablation. *Int J Hyperthermia*. 2010;26(5):499-513.
78. Sebeke LC, Rademann P, Maul AC, et al. Visualization of thermal washout due to spatiotemporally heterogenous perfusion in the application of a model-based control algorithm for MR-HIFU mediated hyperthermia. *Int J Hyperthermia*. 2021;38(1):1174-1187.
79. Karzova MM, Averiyanov MV, Sapozhnikov OA, Khokhlova VA. Mechanisms for saturation of nonlinear pulsed and periodic signals in focused acoustic beams. *Acoust Phys*. 2012;58(1):81-89.

SUPPORTING INFORMATION

Additional supporting information can be found online in the Supporting Information section at the end of this article.

How to cite this article: Gray MD, Spiers L, Coussios CC. Sound speed and attenuation of human pancreas and pancreatic tumors and their influence on focused ultrasound thermal and mechanical therapies. *Med. Phys*. 2024;51:809–825.
https://doi.org/10.1002/mp.16622